ACS OMEGA

http://pubs.acs.org/journal/acsodf

Article

Influence of Capping Ligands, Solvent, and Thermal Effects on CdSe Quantum Dot Optical Properties by DFT Calculations

Didac A. Fenoll, Mariona Sodupe, and Xavier Solans-Monfort*

Cite This: *ACS Omega* 2023, 8, 11467−11478

Read Online

ACCESS | Metrics & More | Article Recommendations | Supporting Information

ABSTRACT: Cadmium selenide nanomaterials are very important materials in photonics, catalysis, and biomedical applications due to their optical properties that can be tuned through size, shape, and surface passivation. In this report, static and ab initio molecular dynamics density functional theory (DFT) simulations are used to characterize the effect of ligand adsorption on the electronic properties of the (110) surface of zinc blende and wurtzite CdSe and a $(CdSe)_{33}$ nanoparticle. Adsorption energies depend on ligand surface coverage and result from a balance between chemical affinity and ligand−surface and ligand−ligand dispersive interactions. In addition, while little structural reorganization occurs upon slab formation, Cd···Cd distances become shorter and the Se−Cd−Se angles become smaller in the bare nanoparticle model. This originates mid-gap states that strongly influence the absorption optical spectra of nonpassivated $(CdSe)_{33}$. Ligand passivation on both zinc blende and wurtzite surfaces does not induce a surface reorganization, and thus, the band gap remains nonaffected with respect to bare surfaces. In contrast, structural reconstruction is more apparent for the nanoparticle, which significantly increases its highest occupied molecular orbital (HOMO)−lowest unoccupied molecular orbital (LUMO) gap upon passivation. Solvent effects decrease the band gap difference between the passivated and nonpassivated nanoparticles, the maximum of the absorption spectra being blue-shifted around 20 nm by the effect of the ligands. Overall, calculations show that flexible surface cadmium sites are responsible for the appearance of mid-gap states that are partially localized on the most reconstructed regions of the nanoparticle that can be controlled through appropriate ligand adsorption.

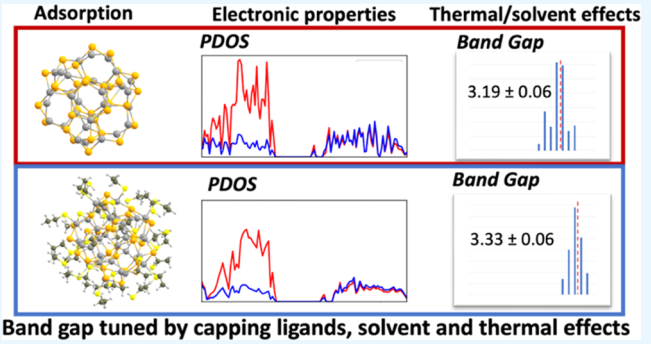

Band gap tuned by capping ligands, solvent and thermal effects

INTRODUCTION

Semiconductor low-dimensional materials (e.g., quantum dots, two-dimensional (2D) single- or few-layered sheets) exhibit different electro-optical properties with respect to their bulk counterparts.[1,2] This has already been exploited in electronic and photonic devices and biological and catalytic applications.[3−14] The enhancement of quantum mechanical effects through spatial confinement and the increase in surface−volume ratio lie behind these novel properties.[2,15] Nanomaterial composition, structure, size, shape, and surface chemistry determine its potential applications, which can be further tailored through various synthetic methods;[16−20] in this regard, low-dimensional CdSe structures have garnered special attention.[21−24] Wurtzite and zinc blende CdSe are the most frequently studied polymorphs. Nanofabrication involving either polymorph requires great control of their growth and surface chemistry to adequately tune their chemical and electro-optical properties.[21−27]

Despite the control of the optical properties that can be achieved through detailed control of the size, shape, and structure of the nanoparticle, quantum dot surface chemistry has emerged as an additional way to tune material properties.[2,17,28,29] Most of the surface atoms are undercoordinated, and this influences their electronic structure, which can result in the presence of hole traps and electronic states in the band gap that ultimately impact the optical properties, often in an undesired manner. In this context, surface passivation appears as a suitable strategy.[29] This passivation can be achieved either by the effect of capping ligands[30−33] or by adding a shell of an inorganic material exhibiting a larger band gap, thus containing the photoprocess in the core.[34−38]

A wide range of ligands has been used for surface passivation. Within the large set of ligands already used, the following groups can be distinguished (Scheme 1): (a) phosphines and phosphine oxide ligands, such as trioctylphosphine and trioctylphosphine oxide; (b) amines and aminoacids, as is the case of dodecylamine; (c) phosphonic and carboxylic acids, including octylphosphonic, oleic, stearic, or 3-

Received: January 16, 2023
Accepted: March 7, 2023
Published: March 17, 2023

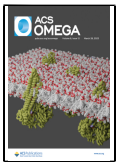

Scheme 1

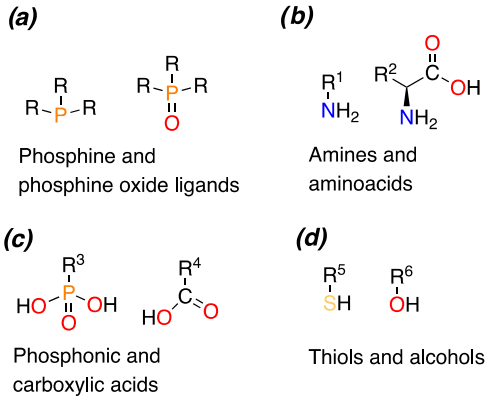

mercaptopropionic acids; and (d) alcohols and thiols, for which decanethiol is the most relevant example. The nature of the capping ligand is important, as it can modify the emission wavelength and/or luminescence quenching.[5,15,17] Understanding the capping ligand interaction and how this interaction influences the adsorption energy and the electronic structure of the surface is of crucial importance for the development of new materials with improved optical properties, and in this context, many experimental[19,20,28,30,32,39−42] and computational contributions[29,41−74] have been reported in the literature.

Density functional theory (DFT) calculations have been carried out to obtain atomistic insights into the ligand−quantum dot surface interaction and how this surface passivation modifies the electronic structure of the material. The influence of surface passivation on the optical properties of the nanomaterial has been examined mainly through three different approaches: (i) analysis of the density of states and/or highest occupied molecular orbital (HOMO)−lowest unoccupied molecular orbital (LUMO) energy difference to determine the effect of the ligands in the band gap;[29,44,45,61,64,73] (ii) time-dependent (TD)-DFT calculations, which allow determining the maximum adsorption and emission wavelength of the nanoparticle in the presence/absence of a particular ligand;[41,48,49,54,55,59,61,64] and (iii) the radiative/nonradiative exciton decay mechanisms and their impact on, for instance, photoluminescence quenching.[50,68] Both slab[29,43−46] and nanoparticle models[41,42,47−61,63−66,68,69,71−75] have already been used in the literature. Indeed, periodic slab models have been used in the characterization of ligand adsorption on selected facets, albeit at the cost of forgoing finer details present in the structure of nanoparticles.[29,43−46] Regarding the modeling with clusters and nanoparticles, much effort has been centered on nanoparticles with up to 30 CdSe units, with $Cd_{13}Se_{13}$ being one of the most employed,[41,47−59] as it has been reported to be a significantly stable cluster according to mass spectrometry experiments.[76] Recently, larger nanoparticle models have been employed by different groups,[42,61−64,66,68−75] which allowed representing the actual size of quantum dots in a more realistic manner as well as analyzing the role of different ligands.

The appearance of trap states on the edges of the band gap region seems to be linked to surface defects with incomplete passivation.[67,69,73] In this context, most of the calculations with a small nanoparticle model (i.e., $(CdSe)_{13}$) agree with the fact that the adsorption of capping ligands modifies the band gap,[48,49,54−56,65] thus leading to shifts in the emission wavelength when compared to ligand-free models. In contrast, controversy exists on calculations performed with larger models. That is, while there is a consensus that both anionic and neutral ligands modify the band gap of large non-stoichiometric nanoparticles,[60,69] the role of neutral ligands on stoichiometric models is less pronounced.[59,61,64,65] In this context, the inclusion of thermal effects on these larger models through ab initio molecular dynamics has been shown to be important for better representing the nanoparticle−ligand interface[60,62,68] and particularly identifying the increase of the band gap upon capping ligand adsorption.[62] Finally, the presence of ligands influences the localization of the frontier orbitals,[29] and it can increase material luminescence through two effects: first, it decreases the rate constant of the nonradiative decay, and second, the presence of electronic states delocalized both on the material surface and the ligand enables new channels for the radiative decay from the excited state.[50]

In this contribution, we use zinc blende and wurtzite slabs as well as a $(CdSe)_{33}$ nanoparticle model to analyze ligand adsorption of small and large models of the most common capping ligands (phosphonic and carboxylic acids, amines, alcohols, and thiols) and its effect on the electronic properties of the material. For that, we analyze for both polymorphs the intrinsic ligand−surface interaction, together with ligand−ligand stabilizing dispersive interactions. Moreover, we describe the importance of thermal effects through ab initio molecular dynamics (AIMD) simulations. To the best of our knowledge, none of the previous contributions included at the same time such a variety of ligands, both surface and nanoparticle models, and the analysis of thermal effects. Results show that ligand adsorption is stronger on zinc blende than that on wurtzite and, regardless of the CdSe polymorph, phosphonic acids and amines interact more strongly with the surface than carboxylic acids, alcohols, and thiols. The impact of ligand adsorption on the electronic structure of the material is determined to be low in rigid systems, such as in crystalline periodic surfaces, yet significant in small nanoparticles. This is related to the different surface reconstructions of the slab models and the nanoparticle in the presence/absence of capping ligands and the appearance/disappearance of mid-gap states on the nanoparticle.

COMPUTATIONAL DETAILS

All calculations were carried out with the VASP code,[77,78] which performs three-dimensional (3D) periodic calculations using plane wave-based basis sets. Therefore, regardless of the dimensionality of the model (3D, 2D, or zero-dimensional (0D)), calculations include periodicity in the three directions. For 2D and 0D systems, the lattice parameters used guarantee a distance between the most external atoms of the images of at least 10 Å in the nonperiodic directions. For the slabs, the c value is 30 or 40 Å depending on the length of the alkyl chain of the ligand. In addition, the $(CdSe)_{33}$ nanoparticle and the associated capped models are included in a 35 Å large cubic box (see below).

Models. The ligand adsorption on CdSe and its effect on the band gap were modeled with both slab and finite nanoparticle model approaches (Figure 1). Regarding the slab models, two different surfaces were considered: stoichiometric (110) zinc blende (ZB) and stoichiometric (110) wurtzite (WZ) surfaces, i.e., the two nonpolar stoichiometric surfaces presenting lower surface energies. Layer-wise surface

https://doi.org/10.1021/acsomega.3c00324
ACS Omega 2023, 8, 11467−11478

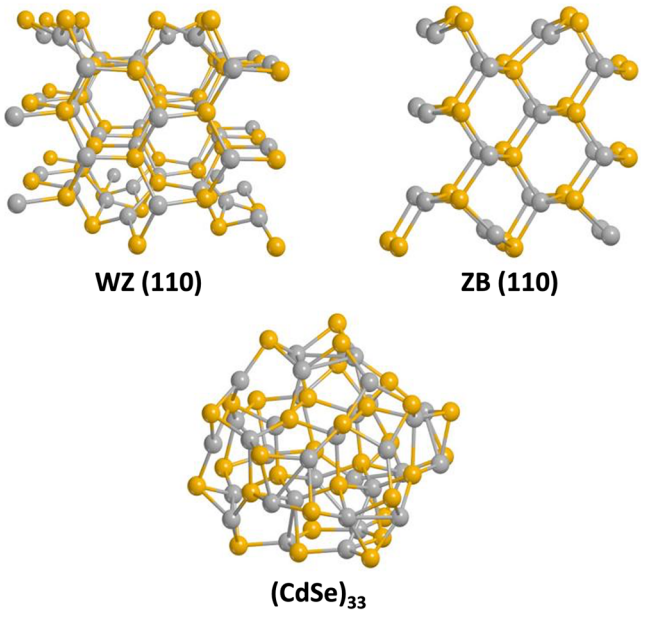

Figure 1. Optimized structures for the unit cells of (110) wurtzite (WZ) and (110) zinc blende (ZB) and for the $(CdSe)_{33}$ nanoparticle model. Cadmium atoms are in gray and selenium atoms are in orange.

energy convergence was used to select slab thickness for both ZB (110) and WZ (110) surfaces (see Figure S1 in the Supporting Information). The role of the CdSe polymorph was analyzed with (3×3) and (2×2) supercells of the (110) ZB and (110) WZ surfaces to ensure the absence of lateral interactions between ligands. Moreover, the importance of ligand coverage on the adsorption energy and the band gap structure was analyzed on the smallest (110) ZB and (110) WZ (1×1) surfaces. Additionally, one nanoparticle model constructed from wurtzite and already used by several authors was also considered.[59,61,62,64,66,72−74] The model is obtained by spherically cutting an extended wurtzite-like crystalline bulk as detailed in previous works.[61] This model includes 33 CdSe units, corresponding to one of the clusters identified by mass spectrometry.[76] Moreover, the nanoparticle model has 27 surface and 6 internal Cd centers, thus it presents 27 vacancies, each being initially saturated with one capping ligand in the calculations representing the full coverage of the nanoparticle. During structure optimizations, all atoms were allowed to relax both on the slab and nanoparticle models; cell parameters were kept fixed in all cases.

The effect of the ligand structure was analyzed by considering four groups of ligands as summarized in Scheme 2: (a) carboxylic acids, (b) phosphine oxides and phosphonic acids, (c) amines, and (d) alcohols and thiols. In each group, small−large pairs of ligands were considered. In the small models, the alkyl chain is CH_3CH_2- (C2), whereas the largest species has $CH_3-(CH_2)_9-$ as an alkyl chain (C10), with few exceptions. Additionally, in the case of the amines and the phosphonic acids, the more sizeable triethyl amine and triethylphosphine oxide ligands were included to analyze how the ligand's steric effects may influence ligand coverage on the surface.

Level of Theory. Geometry optimizations were carried out at the density functional theory (DFT) level using the Perdew−Burke−Erzernhof (PBE) exchange−correlation functional[79] along with Grimme's D2 dispersion[80] correction as

Scheme 2

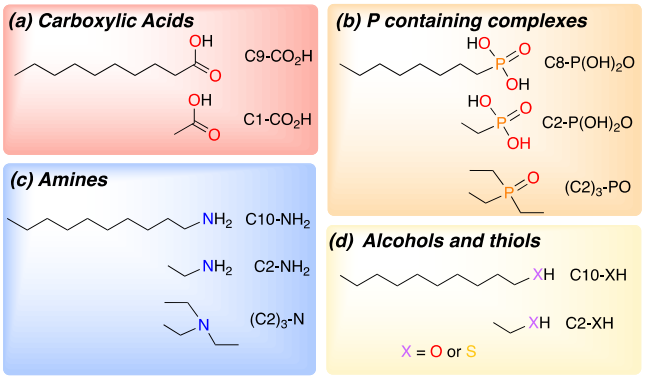

implemented in VASP 5.4. PBE-D2 was used recently in our research group and shown to give cell parameters closer to experiments than PBE-D3.[81,82] Spin-polarized calculations were performed for bulk and pristine surfaces to successfully confirm the absence of magnetization. Therefore, all other systems and the results reported hereafter are based on non-spin-polarized calculations. The atomic ionic cores were represented with projector augmented wave (PAW) pseudopotentials[83,84] and the valence electrons were represented with a plane wave basis set with a 500 eV cutoff. For each system, different Monkhorst−Pack[85] reciprocal space *k*-point grids were employed depending on cell dimensions to ensure efficient cost−accuracy simulations (Figures S2 and S3 in the Supporting Information). The nanoparticle model was computed at the Γ point due to its nonperiodic nature. For the zinc blende (110) slab, 2×2×1 and 8×8×1 meshes were employed for ZB(3×3) and ZB(1×1) cells, respectively. For the wurtzite (110) facet, 2×2×1 and 4×4×1 meshes were used for WZ(2×2) and WZ(1×1), respectively, owing to its larger unit cell parameters. Bader charge analysis[86,87] was performed to analyze charge transfer between ligands and the CdSe material.

Since generalized gradient approximation (GGA) functionals tend to underestimate semiconductor band gaps, two main strategies have been proposed to overcome this limitation: (a) the use of hybrid functionals and (b) the inclusion of Hubbard's correction (*U*). For the case of CdSe, the hybrid PBE0 density functional has been shown to be appropriate,[47,58] and also, other authors applied Hubbard's correction with success.[88] In this context, we decided to analyze the optical properties of the different CdSe-based materials using three different levels of theory: PBE, PBE-*U*, and PBE0. For that, we first calibrated the U_{eff} value following the Dudarev et al. scheme[89] by trying to reproduce the band gap of CdSe zinc blende bulk. We found that a U_{eff} of 14 eV at Cd d orbitals was necessary to obtain reasonably accurate band gaps (see Figure S4 in the Supporting Information). We also analyzed the dependence of the band gap on the Monkhorst−Pack mesh density (Figures S2 and S3 in the Supporting Information) and found that 32×32 × 32 and 32× 32 × 1 meshes for the bulk and surface models, respectively, warranted band gap convergence with respect to Brillouin zone representation. Unfortunately, such dense Monkhorst−Pack meshes are impractical with PBE0, which requires sparser grids. Results for ZB and WZ bulk and surfaces as well as the $(CdSe)_{33}$ nanoparticle using PBE, PBE + *U*, and PBE0 at the

https://doi.org/10.1021/acsomega.3c00324
ACS Omega 2023, 8, 11467−11478

PBE-D2 optimized geometries are reported in Table 1 (and Table S1 in the Supporting Information (SI)).

As expected, PBE values are systematically lower than PBE0 and PBE-*U* values. However, while the difference between PBE and PBE0 with the same number of *k*-points is constant (1.42−1.47 eV) regardless of the material considered, the difference between PBE and PBE-*U* decreases significantly with the decrease of material dimensionality. Moreover, experimental data for $(CdSe)_{33}$ suggest that the band gap of this cluster should be around 3.0 eV,[76] something that is not well reproduced with PBE-*U*. This so large U_{eff} value also modifies the orbitals contributing to the valence and conducting bands, the contribution from cadmium 4d orbitals to the conduction band becoming not negligible. Therefore, our data suggest that PBE-*U* is not a good strategy for analyzing the electronic structure of CdSe nanoparticles and should be avoided in these kinds of systems. So, our best estimated band gap values (BEV) are obtained by adding 1.45 eV (mean difference between PBE and PBE0 values with the same number of *k*-points) to PBE band gaps with the larger number of *k*-points.

In addition, we analyzed the effect of solvent on the band gap by including it implicitly with VASPSOL.[90] We consider water solvent as the limiting case, but test calculations with toluene and acetonitrile (Table S2 in the Supporting Information) show that the effects observed with water (see below) can be tuned by modifying solvent polarity.

Thermal effects on the full coverage nanoparticle $[(CdSe)_{33}-L_{27}]$(L = capping ligand) models were taken into account by performing NVT ab initio molecular dynamics. A Nosé−Hoover thermostat, set at 300 K, was used.[91,92] An optimized structure for each capping ligand was taken as the initial structure in a 0.5 ps equilibration simulation. Once thermalization ensued, 1000 steps (1 ps) of AIMD were used for clusterization. This clusterization was performed with the algorithm provided in UCSF Chimera[93] and considering the Cd center distribution. The most representative structures resulting from clusterization were used to analyze the thermal effects on full coverage nanoparticle optical properties.

Finally, to further analyze the optical properties of the $(CdSe)_{33}$ passivated and nonpassivated nanoparticles, we performed TD-DFT calculations on structures obtained during the AIMD simulation at the PBE0 level of theory as implemented in the Gaussian 16 package.[94] Atoms were represented with def2-SVP basis sets[95] and the corresponding pseudopotentials.[96] Solvent effects were included with the CPCM continuum model[97,98] and considering water as the solvent. The reported absorption spectra are obtained by considering three representative structures of the AIMD simulation: (i) the structure presenting the lowest band gap; (ii) the structure with the highest band gap; and (iii) the structure with the closest band gap to the weighted average value. In each case, we considered the first 10 excited singlet states, and the intensity is computed considering both the oscillator strength and the number of structures of each cluster. To ensure that our approach is reasonable, Figure S5 compares the absorption spectrum of the nonpassivated nanoparticle in vacuum considering the representative structure of all clusters arising from the dynamics with that considering the extrema exclusively, and the results are reasonably similar.

Table 1. Band Gap Energies (in eV) for Zinc Blende (ZB), Wurtzite (WZ) Bulks, ZB (110) and WZ (110) Pristine Surfaces, and $(CdSe)_{33}$ Nanoparticle Model Computed with Different Levels of Theory. BEV Stands for Best Estimated Value

	PBE	PBE-*U*	PBE0	BEV[g]
ZB	0.66[a]	1.56[a]	2.49[d]	2.08
WZ	0.78[a]	1.65[a]	3.09[d]	2.24
(110)ZB	1.21[b]	1.92[b]	2.99[e]	2.66
(110)WZ	1.34[b]	2.01[b]	3.28[f]	2.79
$(CdSe)_{33}$	1.61[c]	1.76[c]	3.08[c]	3.06

[a]Band gaps obtained with a 32×32×32 *k*-point mesh. [b]Band gaps obtained with a 32×32×1 *k*-point mesh. [c]Band gap at the Γ point. [d]Band gaps obtained with an 8×8×8 *k*-point mesh. [e]Band gaps obtained with an 8×8×1 k-point mesh. [f]Band gaps obtained with a 4×4×1 *k*-point mesh. [g]Best estimated value is obtained by adding the difference between PBE and PBE0 with the number of *k*-points used in the optimization to the PBE value with the largest number of *k*-points. BEV stands for best estimated value.

RESULTS AND DISCUSSION

Results are organized into four subsections. We first characterize the pristine structures of zinc blende and wurtzite CdSe bulk, the associated main stoichiometric surfaces, and the $(CdSe)_{33}$ nanoparticle model. In the second stage, we analyze the intrinsic ligand−material interaction and the corresponding adsorption energy on the slab at low coverages. We considered the ligands reported in Scheme 2 and the largest supercell of each surface. We paid attention to the role of the functional group of the capping ligand, the chain length, and the structure of the material. Afterward, we study the adsorption of the ligands considering full coverage to determine the cooperative/competitive effects and the ligand−ligand interactions. Finally, we discuss the band gap shifts induced by the presence of a full layer of ligands on the surface of the slabs and the nanoparticle model. We first present the results from static calculations in vacuum, and then we consider the influence of solvation and thermal effects on the band gap.

CdSe Bulk, Surfaces, and Nanoparticles. The structural properties of bulk zinc blende and wurtzite CdSe, the largest optimized pristine (110) zinc blende and (110) wurtzite surfaces (ZB(3×3) and WZ(2×2), respectively) and the $(CdSe)_{33}$ nanoparticle model are examined first. Table 2 summarizes the cell parameters and the Cd−Se and Cd···Cd distances; Figure 1 shows the optimized structures.

Table 2. PBE-D2 Cell Parameters and Cd−Se Distances (in Å) for Zinc Blende and Wurtzite Structures and the (110) Main Crystallographic Facet of Each Polymorph[a]

model	cell parameters	*d*(Cd−Se)	*d*(Cd−Cd)
WZ	*a* = 4.394 (4.299) *c* = 7.171 (7.010)	2.648	4.322
ZB	*a* = 6.022 (6.017) *b* = 6.022 (6.017)	2.647	4.323
WZ (110)	*a* = 14.095 *b* = 14.936	2.590[b]/2.660[c]	3.818
ZB (110)	*a* = 8.623 *b* = 12.195	2.612[b]/2.657[c]	3.712
$Cd_{33}Se_{33}$	-	2.677[b]/2.667[c]	3.16/3.42

[a]X-ray-determined values are added in parenthesis. [b]Surface atoms. [c]Internal atoms.

https://doi.org/10.1021/acsomega.3c00324
ACS Omega 2023, 8, 11467−11478

Table 3. Surface Cd−Capping Ligand X Distances (in Å) and Adsorption Energies (in kJ mol^{-1}) on (110) Zinc Blende and (110) Wurtzite Surfaces[a]

		low coverage				full coverage			
		ZB(3×3)		WZ(2×2)		ZB(1×1)		WZ(1×1)[b]	
type	ligand	d(Cd−X)	ΔE	d(Cd−X)	ΔE	d(Cd−X)	ΔE	d(Cd−X)	ΔE
R−CO_2H	C9−CO_2H	2.415	−83.2	2.446	−63.2	2.415	−113.5	2.534/2.472	−99.7
	C1−CO_2H	2.400	−81.1	2.417	−70.1	2.425	−79.2	2.432/2.427	−73.1
R−P(X)$_2$O	C8−P(OH)$_2$O	2.287	−111.7	2.309	−97.7	2.301	−106.6	2.574/2.610	−144.4[d]
	C2P(OH)$_2$O	2.292	−125.9	2.330	−94.4	2.501	−85.2	2.396/2.524	−129.3
	(C2)$_3$−PO	2.297	−130.2	2.305	−123.1	--[c]	--[c]	--[c]	--[c]
R−NX_2	C10−NH_2	2.353	−112.7	2.380	−99.6	2.427	−141.3	2.397/2.403	−134.7
	C2−NH_2	2.363	−117.3	2.364	−107.0	2.386	−111.0	2.395/2.389	−105.2
	(C2)$_3$−N	2.550	−49.6	4.177	−54.1	--[c]	--[c]	--[c]	--[c]
R−OH	H−OH	2.447	−62.7	2.485	−61.3	2.499	−66.2	2.474/2.489	−58.6
	C10−OH	2.397	−80.2	2.412	−65.3	2.631	−109.3	2.463/2.477	−114.0
	C2−OH	2.405	−83.0	2.428	−74.4	2.486	−81.1	2.464/2.473	−75.7
R−SH	C10−SH	2.730	−76.0	2.745	−65.0	2.815	−112.6	2.851/2.790	−100.5
	C2−SH	2.722	−73.0	2.769	−66.1	2.813	−85.7	2.811/2-800	−75.3

[a]Low and full coverage of the ligands are considered. [b]Only the most stable configuration is reported. [c]The unit cell is too small to accommodate the ligands in the full coverage situation. [d]The most stable adsorption mode for C8−P(OH)$_2$O differs from all other situations.

PBE-D2 optimizations lead to cell parameters that are very close to the experimentally determined values for ZB and WZ. Indeed, the largest deviation is 0.16 Å for the largest c value of wurtzite. Furthermore, the computed Cd−Se and Cd−Cd distances in ZB and WZ bulk are in very good agreement with experimental values (see Table 2). Overall, this indicates that the methodology used is accurate enough for structure characterization. The Cd−Se of the slab models is similar to that of bulk, with major differences observed only for the surface atoms. This leads to a shorter surface Cd···Cd distance of about 3.7−3.8 Å. In contrast, a large reorganization is observed on the nanoparticle model, particularly at the surface, where several Cd−Cd interactions with much smaller distances and smaller Se−Cd−Se angles are observed (Table 2).

Bader charge analysis (Table S3 in the Supporting Information) provides very similar values both for ZB and WZ CdSe bulk. These charges are not homogeneous in the slab models. The outermost Se and Cd atoms present a lower charge separation (−0.66 in ZB (110) and WZ (110)) than the inner centers, whose values are closer to those of the bulk (−0.71 and −0.72 for ZB and WZ bulk structures, respectively). Consistently, Se atoms are Lewis bases and Cd atoms are Lewis acids, and as such ligands preferentially bind to surface Cd sites.

Low Surface Coverage Ligand Adsorption. Adsorption of capping ligands occurs mainly by the interaction of the basic heteroatom of the ligand with Cd surface atoms (perpendicular adsorption). At low coverages, an alternative adsorption mode in which the capping ligand alkyl chain interacts with the surface through dispersion interactions is also plausible (parallel mode). First, we evaluated the intrinsic interaction between the ligand and the surface; that is, we considered large zinc blende (3 ×3) and wurtzite (2×2) surface models to avoid lateral ligand interactions. We considered the different adsorption modes (perpendicular and parallel) for all ligands shown in Scheme 2. Table 3 summarizes the Cd−capping ligand distance and the adsorption energies on ZB(3×3) and WZ(2×2) through the perpendicular mode. Figure 2 shows the optimized structure for the perpendicular adsorption of the smaller ligand of each type. All other structures can be found in the Supporting Information (Figures S6−S12).

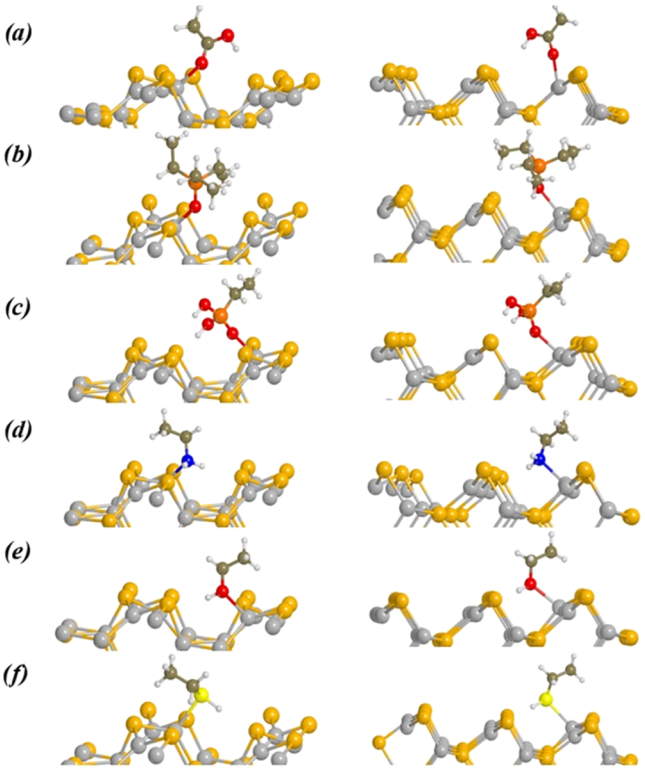

Figure 2. Low-coverage ligands adsorbed on WZ22 (left) and ZB33 (right), including (a) acetic acid, (b) ethylphosphonic acid, (c) trimethylphosphine oxide, (d) ethylamine, (e) ethanol, and (f) ethanethiol.

The adsorption through the perpendicular coordination mode takes place in a very similar manner regardless of the ligand type. The ligand adsorbs through the coordination of the X atom to Cd, the Cd···X distances varying between 2.287 and 2.769 Å. According to Bader charge analysis (Table S4 in the Supporting Information), the interaction is electrostatic with negligible charge transfer. However, the alkyl chain is in all cases slightly tilted due to dispersive interactions between the alkyl chain and the surface. A comparison between the

https://doi.org/10.1021/acsomega.3c00324
ACS Omega 2023, 8, 11467−11478

different types of ligands shows that for the two surfaces, the shortest Cd···X distances correspond to the phosphonic acid and phosphine oxide type species, whereas the largest values are obtained for thiols. Furthermore, R−SH and R−OH ligands can additionally form hydrogen bond contacts with the surface selenium atoms. However, the H···Se distance varies from 2.297 to 2.992 Å, showing that hydrogen bonding between the ligands and the surface is weak. Moreover, we explored the possibility of proton transfer between these ligands and the surface, but most attempts evolved toward the molecular form and when we succeed to obtain the dissociated form, this structure lies very high in energy. The parallel adsorption mode presents systematically larger Cd···X distances (by around 0.02 Å). The alkyl chain and the surface distances are around 3−4 Å, indicative of an alkyl chain−surface dispersive interaction. Overall, the local Cd···X interaction is weakened to reinforce the alkyl chain−surface dispersion.

The adsorption energies through the perpendicular mode range between −130.2 and −61.3 kJ mol^{-1}, with the exception of $(C2)_3N$ that presents lower adsorption energies (in absolute value) as a consequence of the absence of a direct N···Cd interaction. Comparison between the computed values allows establishing the three following trends. First, the adsorption energy of the small and large analogous ligands differs by less than 13.0 kJ mol^{-1}, with most cases being between 1.3 and 6.6 kJ mol^{-1}. This suggests that lateral interactions are negligible and thus no dispersion interactions between alkyl chains exist in these large supercells. Second, the strongest adsorption energies are computed for phosphonic acid, phosphine oxide, and primary amine ligands, and the weakest are associated with carboxylic acids, alcohols, and thiols. The specific ordering for the lighter models is $(C2)_3PO$ > $(C2)P(OH)_2O$ ∼ $(C2)NH_2$ > (C1)COOH ∼ (C2)OH ∼ (C2)SH, in agreement with the proton affinity trends of the different ligands that can also be classified in these two major groups (Table S5 in the Supporting Information). Third, the adsorption energies on the zinc blende surface are systematically higher than those computed on the wurtzite slab by about 30.2−5.8 kJ mol^{-1} (most values range from 10.9 to 15.1 kJ mol^{-1}). These higher adsorption energies for ZB are attributed to larger surface−ligand dispersive interactions due to surface morphology. Indeed, while the adsorption energies without Grimme's dispersion term are very similar for both surfaces, the dispersive contribution to the adsorption energy is 11.1−25.0 kJ mol^{-1} larger in ZB than that in WZ (see Table S6 in the SI).

The adsorption energies through the parallel mode range between −142.6 and −87.7 kJ mol^{-1} (see Table S7 in the SI) and they are systematically higher than those of the perpendicular mode. Thus, despite the fact that this adsorption mode implies a decrease in the direct Cd···X interaction (enlargement of the Cd−X distance of about 0.1−0.4 Å), it is compensated by the alkyl chain−surface interaction through dispersion. In this context, results suggest that at low coverages, ligands will mainly adopt a conformation that maximizes the interaction of the alkyl chain with the surface, regardless of the functional group.

Full Surface Coverage Ligand Adsorption. Once the main factors determining the intrinsic ligand−CdSe surface interaction are determined, we address the ligand full coverage defined as the adsorption of one ligand per surface cadmium cation. This is the model that best reproduces the experimental conditions and represents ligand−ligand interactions. We used the smallest (110) WZ (1×1) and (110) ZB(1×1) cells, which enclose two and one cadmium surface cation, respectively. Table 3 reports the adsorption energies of the most favorable conformation for all ligands shown in Scheme 2. Figure 3 shows the optimized structures for all considered conformations for the decanoic acid, decanol, and decanethiol. Note that for the case of the (110) WZ (1×1) surface, we explored different ligand adsorption modes to determine how the interaction between two ligands that are not related by translational symmetry may affect the adsorption on the surface.

The ligand adsorption on the (110) ZB (1×1) surface takes place through the perpendicular mode similar to the

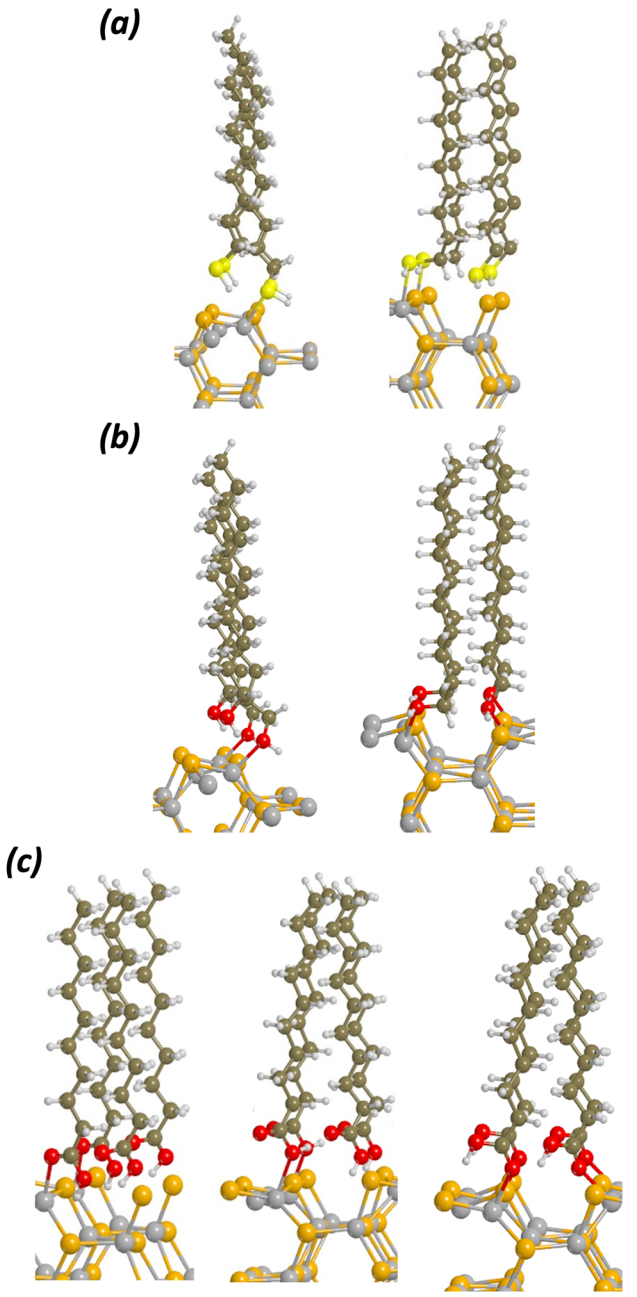

Figure 3. Optimized structures of the different conformations resulting from full coverage ligands adsorption on the WZ (1×1) surface: (a) decanethiol, (b) decanol, and (c) decanoic acid.

https://doi.org/10.1021/acsomega.3c00324
ACS Omega 2023, 8, 11467−11478

perpendicular mode of the isolated ligands. The only exceptions are $(C2)_3PO$ and $(C2)_3N$ ligands, which are too large to fit inside the (110) ZB (1×1) unit cell. This outlines that these two ligands and their associated families (phosphine oxides and tertiary amines) are not suitable for saturating all cadmium vacant sites. The Cd···X distance in the full coverage is akin to that of the low coverage, albeit slightly larger in general. The Cd···X distance trends are the same as those observed for the isolated systems ($(C2)P(OH)_2O$ < $(C2)NH_2$ < (C1)COOH < (C2)OH < (C2)SH). This suggests that the ligand−surface interaction is similar to that in the low-coverage simulation with minimum competitive effects. As a consequence, the adsorption energies can again be divided into the same two groups as in the low-coverage scenario: those of phosphonic acid and amine ligands, which are systematically adsorbed more strongly for a fixed alkyl chain length, and those of carboxylic acids, alcohols, and thiols. The adsorption energies at full coverage for the smallest C2 models on ZB are in general close to those of the low coverage, the largest deviation being between −10.0 and +12.7 kJ mol^{-1}. In contrast, the adsorption energy for the largest models is systematically larger than the value for the low coverage by about 30 kJ mol^{-1} (range 28.6−36.6 kJ mol^{-1}). Since the Cd··· X distance does not vary significantly, this arises from the dispersive stabilizing ligand−ligand interactions, which are particularly important in the large models. Indeed, calculations for several thiols with increasing alkyl chains show that the ligand−ligand stabilizing interaction increases by about 5.2 kJ mol^{-1} per CH_2 (Figure S13).

In the case of the (110) WZ surface, the presence of two ligands per unit cell gives rise to a larger configurational variability. That is, for thiols, alcohols, and amines, we have identified two different modes of adsorption: one in which the two ligands interact with cadmium atoms, and another one where one ligand is directly adsorbed on the surface, while the latter is hydrogen-bonded to the former (Figure 3a,b). Meanwhile, for carboxylic and phosphonic acids, there are five potential different coordination modes depending on whether the adsorption of each ligand takes place through the =O group or the OH and the number of ligands directly adsorbed (1 or 2). However, some of these possibilities were not stable and during the optimization evolved to one of the other conformations (Figure 3c). In all cases, the most stable configuration is that where the two ligands interact with the surface, although the configuration where one ligand is desorbed, and hydrogen bonded with the other ligand has an adsorption energy per ligand that is only between 3.1 and 17.4 kJ mol^{-1} lower in absolute value (adsorption energies for all conformations are reported in Table S8 in the Supporting Information). Moreover, for the acids, the preferred adsorption mode is through the =O group by at least 5.5 kJ mol^{-1} per ligand. Finally, as for ZB, adsorption energies for the long-alkyl-chain ligands are systematically larger by 35−50 kJ mol^{-1} due to ligand−ligand interactions. This increase is larger than in ZB due to a shorter surface Cd···Cd distance in WZ, which favors lateral dispersive interactions. As a result, adsorption energies on ZB and WZ at full coverages become more similar.

Optical Properties. As mentioned in the introduction, CdSe quantum dots show excellent optical properties for a large variety of applications such as optical devices, photocatalysis, and biomedical diagnosis.[3−14] Ligand passivation can tune the electronic structure of the material; thus, we analyzed how the adsorbed ligands modify the band gap for the slab models and the $(CdSe)_{33}$ nanoparticle at full coverage. Table 4 reports the band gap of the pristine (110) ZB and (110) WZ slab models, and the pristine $(CdSe)_{33}$ nanoparticle as well as those of the passivated systems with the smaller model of each type of ligands considered. Figure 4 shows the projected density of states (pDOS) of the pristine materials (bulk, surfaces, and nanoparticle) and the pDOS of $(CdSe)_{33}$ capped with 27 ethanethiol molecules ($Cd_{33}Se_{33}$-27EtSH), centered around the band gap region.

The estimated band gap energies of the pristine models vary between 2.08 and 3.06 eV depending on the model (bulk, slab, or nanoparticle) and the polymorph considered. The band gap for ZB bulk is 0.12 eV smaller than that of the WZ polymorph.[27,99−101] This agrees with the lower band gap experimentally determined for ZB, albeit both absolute band gaps are 0.3−0.4 eV higher than those determined experimentally. The band gap energies of the slab models and the $(CdSe)_{33}$ nanoparticle are higher than those of the bulk structures, consistent with a decrease in the dimensionality of the system. The projected density of states (pDOS) indicates that the valence band for all materials is mainly formed by selenium 4p orbitals, while the conducting band has contributions of both cadmium 5s and selenium 4p orbitals. Due to the different dimensionalities of the systems, the conducting and valence band edge states appear at different energies for each system. However, when referenced to the Fermi level, the pDOS of bulk and slab models are relatively similar and none of them presents mid-gap states (Figure 4a−d). In contrast, the pDOS of the nanoparticle model (Figure 4e) is significantly different and is characterized by the presence of mid-gap states. The presence of these mid-gap states arises from the nanoparticle reconstruction that leads to short Cd···Cd distances and small Se−Cd−Se angles.

Adsorption of capping ligands on both ZB and WZ surface models does not significantly alter the band gap, with almost all differences being within 0.04 eV. This is linked to a lowly reorganization of the surface Cd···Cd distances. In contrast, adsorption on the nanoparticle induces an increase of the band gap by at least 0.2 eV. In particular, the computed value for $(CdSe)_{33}$−$(C2-NH_2)_{27}$ is 3.44 eV in reasonable agreement with the reported adsorption spectrum of this cluster with decylamine in toluene (λ = 415 nm).[76] Indeed, the band gap obtained from calculations correctly accounts for the differences between the materials studied here, but it is 0.4 eV higher than that of the experiments as already found for bulk materials. Remarkably, TD-DFT calculations (Table S9 in the Supporting Information) at the PBE0/def2-SVP level of theory suggest that the experimental and computational discrepancy does not arise from the selected functional but from the fact

Table 4. Best Estimated (See the Computational Details Section) Band Gap Energies in the Gas Phase and Water (in eV) for Pristine and Passivated Slab and Nanoparticle Models

	ZB (110)		WZ (110)		$(CdSe)_{33}$	
	Gp	water	Gp	water	Gp	water
pristine	2.66	2.67	2.79	2.84	3.06	3.43
C2−COOH	2.64	2.60	2.81	2.77	3.25	3.49
$C2-NH_2$	2.65	2.58	2.82	2.76	3.44	3.51
C2−OH	2.56	2.55	2.83	2.83	3.30	3.43
C2−SH	2.70	2.65	2.83	2.79	3.42	3.49

https://doi.org/10.1021/acsomega.3c00324
ACS Omega 2023, 8, 11467−11478

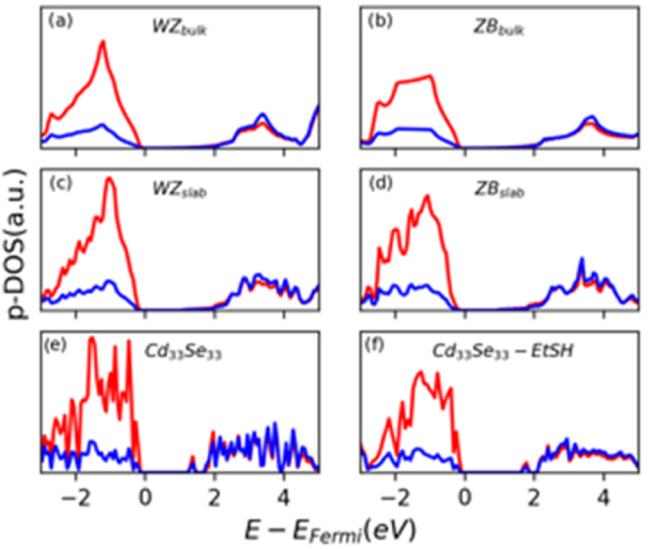

Figure 4. Projected density of states (Cd blue line, Se red line) of wurtzite (a) and zinc blende (b) bulk, the main (110) wurtzite (c) and zinc blende surfaces (d), the $(CdSe)_{33}$ nanoparticle model (e), and the $(CdSe)_{33}$ nanoparticle with 27 C2−SH ligands adsorbed on its surface (f).

that we are analyzing the band gap instead of the optical transitions. The band gap increase is related to the displacement of the mid-gap states to higher values with respect to the Fermi Level due to the interaction between the nanoparticle and the capping ligand (Figure 4).

The inclusion of solvent effects at the gas-phase-optimized structures using an implicit continuum model has little influence on the band gap of pristine and passivated surfaces (±0.06 eV). Consequently, the computed band gaps with and without surface passivation are very similar and suggest that in the absence of surface reconstruction, neither solvation nor ligand passivation tunes the band gap. On the other hand, solvent effects have a large influence on the band gap of the pristine nanoparticle that becomes 3.43 eV in water solution (3.06 eV in the gas phase). The presence of ligands passivating $(CdSe)_{33}$ diminishes the influence of the solvent regardless of the nature of the ligand, and thus, the band gap of the passivated nanoparticles only increases by about 0.1−0.2 eV. Overall, the band gaps of the nonpassivated and passivated nanoparticles become very similar in water. Similar trends are found when considering less polar solvents (acetonitrile or toluene, Table S2 in the Supporting Information), but the effect is less pronounced.

Finally, since the results obtained from static calculations show that the band gap of the nanoparticle is very sensitive to solvation as well as its structure, subtle changes associated with thermal effects may influence the band gap and the role of capping ligands. To evaluate these thermal effects, ab initio molecular dynamics calculations have been performed for the five nanoparticle models: pristine $CdSe_{33}$, $CdSe_{33}-(C2COOH)_{27}$, $CdSe_{33}-(C2NH_2)_{27}$, $CdSe_{33}-(C2OH)_{27}$, and $CdSe_{33}-(C2SH)_{27}$. For each trajectory, clusterization based on the cadmium centers has been performed and the band gap of the representative structure of each cluster has been computed with and without solvation. In addition, we computed the

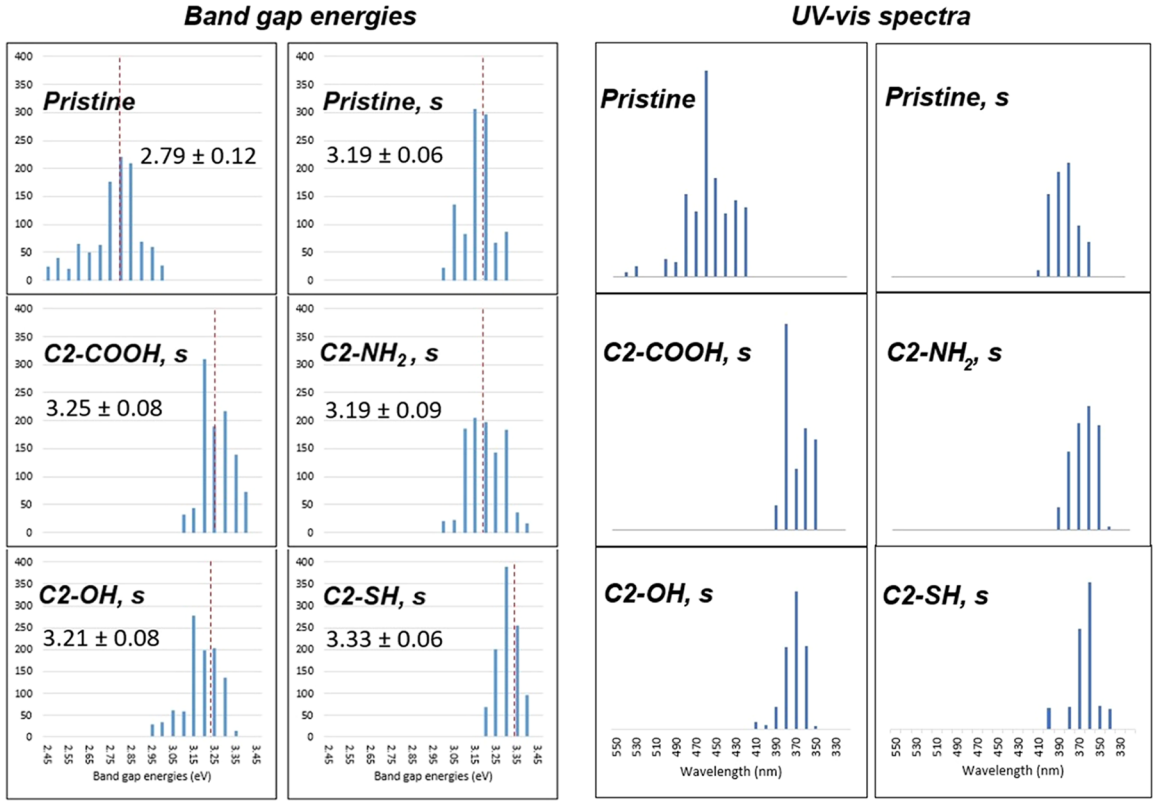

Figure 5. Weighted band gap and UV−vis spectra of the representative AIMD structures of pristine $(CdSe)_{33}$ (with [s] and without solvation) and the full covered nanoparticle models with 27 acetic (C2−COOH), ethylamine (C2−NH2), ethanol (C2−OH), and ethanethiol (C2−SH) capping ligands.

https://doi.org/10.1021/acsomega.3c00324
ACS Omega 2023, 8, 11467−11478

absorption spectra of these systems by considering 10 excited states of three representative structures (see the Computational Details section). Results show that the band gap energy values as well as the absorption wavelengths are sensitive to the structure of the nanoparticle (Figure 5), with variations being as large as 0.5 eV (120 nm) in agreement with the work of Tretiak and co-workers.[62] Remarkably, the band gap fluctuation decreases significantly both by ligand adsorption and the inclusion of solvent effects, the latter factor being predominant. Similarly, the bandwidth of the absorption spectra decreases when including solvent effects. Moreover, the weighted band gaps are smaller than those of the static calculations due to the changes in the HOMO and LUMO energies associated with the general increase of the bond distances. Interestingly, the inclusion of thermal effects does not change the trends observed in the static calculations as evidenced by the following two observations. First, even though the difference between the pristine and passivated nanoparticles is smaller than the static calculations, there is an increase in the gas phase band gap upon adsorption of 27 capping ligands. Second, addition of solvent effects increases the weighted band gap of the pristine nanoparticle significantly but almost does not modify that of the passivated models. Overall, the maximum wavelength of the absorption spectra of the solvated pristine nanoparticle is blue-shifted by 80 nm when compared to the values in vacuum, while the difference between the maximum absorption wavelength of passivated and nonpassivated nanoparticles including solvation is 20 nm.

CONCLUSIONS

Cadmium selenide nanoparticles are among the most widely used quantum dots in photonics, solar cells, catalysis, and bioimaging. Surface passivation through the adsorption of capping ligands is key for tuning the quantum dot's optical properties, and atomistic insights into how ligand alters their properties are important for the design of new quantum dots. The present computational work provides a broad, comprehensive insight into the ligand passivation on CdSe nanomaterials through a combination of static and AIMD DFT simulations. The zinc blende (ZB) and wurtzite (WZ) (110) surfaces, the $(CdSe)_{33}$ nanoparticle, and five types of ligands used in experiments (carboxylic acids, phosphonic acids, amines, alcohols, and thiols) were considered to analyze how their adsorption influences the optical properties of the material.

Ligand adsorption is mainly electrostatic with almost no charge transfer from the ligand to the surface. At low coverages, ligand adsorption energies on ZB are computed to be higher than those on WZ by about 10−15 kJ mol^{-1} due to the larger surface−ligand dispersive interactions. Moreover, for both polymorphs, phosphine oxides, phosphonic acids, and amines adsorb more strongly than carboxylic acids, alcohols, and thiols, and this correlates well with their proton affinities, reinforcing the electrostatic nature of the interaction. Increasing the ligand coverage up to full coverage does not change the trends found at low coverages. However, the steric hindrance of phosphine oxides and tertiary amines hampers their adsorption on each undercoordinated surface Cd site. Moreover, the adsorption difference between ZB and WZ decreases due to larger ligand−ligand dispersive interactions in the latter. Indeed, dispersive ligand−ligand interactions are important for large ligands mainly, and their contribution is estimated to be about 5.2 kJ mol^{-1} per CH_2 unit.

Results on the optical properties of bare materials (bulk, surfaces, and nanoparticles) show that decreasing model dimensionality on going from bulk to surfaces and nanoparticles increases the energy band gap. However, the density of states of the $(CdSe)_{33}$ nanoparticle presents mid-gap states that decrease the overall HOMO−LUMO energy difference. These mid-gap states arise from the nanoparticle reconstruction that leads to shorter Cd···Cd distances and smaller Se−Cd−Se angles. Ligand passivation on both zinc blende and wurtzite surfaces is not associated with an important surface reconstruction and, consequently, the band gap is very similar to that of the bare surfaces. In contrast, ligand adsorption on $(CdSe)_{33}$ induces a significant structural reconstruction, which is related to a general increase of the Cd···Cd distances. Therefore, mid-gap states move to higher energies so that the HOMO−LUMO gap increases, and the maximum of the absorption spectrum is blue-shifted upon passivation.

Overall, the combination of slab and nanoparticle models suggests that while rigid and crystalline unsaturated cadmium atoms (represented with the slab models) are essentially not affected neither by the adsorption of organic ligands nor the solvent effects, centers located at flexible environments (represented by $(CdSe)_{33}$) are more sensitive to the presence of both the capping ligands and the solvent, although the effects do not depend on the nature of the capping ligand. This makes the tunning of the optical properties through ligand passivation rather limited. Thus, passivation through core−shell materials and nanoparticle size appears to be more suitable strategies.

ASSOCIATED CONTENT

Supporting Information

The Supporting Information is available free of charge at https://pubs.acs.org/doi/10.1021/acsomega.3c00324.

All calibration tests for defining the computational methodology; adsorption energies for the parallel mode as well as for the different conformations of the WZ full coverage scenario; TD-DFT calculations; and the crude data of the AIMD simulations (PDF)

AUTHOR INFORMATION

Corresponding Author

Xavier Solans-Monfort − *Departament de Química, Universitat Autònoma de Barcelona, 08195 Bellaterra, Spain;* orcid.org/0000-0002-2172-3895; Email: xavier.solans@uab.cat

Authors

Didac A. Fenoll − *Departament de Química, Universitat Autònoma de Barcelona, 08195 Bellaterra, Spain;* orcid.org/0000-0003-1141-8114

Mariona Sodupe − *Departament de Química, Universitat Autònoma de Barcelona, 08195 Bellaterra, Spain;* orcid.org/0000-0003-0276-0524

Complete contact information is available at: https://pubs.acs.org/10.1021/acsomega.3c00324

Notes

The authors declare no competing financial interest.

https://doi.org/10.1021/acsomega.3c00324
ACS Omega 2023, 8, 11467−11478

■ ACKNOWLEDGMENTS

The authors gratefully acknowledge financial support from MICINN [PID2020-112715GB-I00], the Generalitat de Catalunya [2017SGR1323]. D.A.F. acknowledges MICINN for his FPU PhD fellowship [FPU18/03612]. X.S.-M. is grateful for Professor Agregat Serra Húnter position.

■ REFERENCES

(1) Alivisatos, A. P. Semiconductor Clusters, Nanocrystals, and Quantum Dots. *Science* **1996**, *271*, 933−937.
(2) Boles, M. A.; Ling, D.; Hyeon, T.; Talapin, D. V. The Surface Science of Nanocrystals. *Nat. Mater.* **2016**, *15*, 141−153.
(3) Polman, A.; Knight, M.; Garnett, E. C.; Ehrler, B.; Sinke, W. C. Photovoltaic Materials: Present Efficiencies and Future Challenges. *Science* **2016**, *352*, No. aad4424.
(4) Yang, Y.; Zheng, Y.; Cao, W.; Titov, A.; Hyvonen, J.; Manders, J. R.; Xue, J.; Holloway, P. H.; Qian, L. High-Efficiency Light-Emitting Devices Based on Quantum Dots with Tailored Nanostructures. *Nat. Photonics* **2015**, *9*, 259−265.
(5) Carey, G. H.; Abdelhady, A. L.; Ning, Z.; Thon, S. M.; Bakr, O. M.; Sargent, E. H. Colloidal Quantum Dot Solar Cells. *Chem. Rev.* **2015**, *115*, 12732−12763.
(6) Kamat, P. V. Quantum Dot Solar Cells. The next Big Thing in Photovoltaics. *J. Phys. Chem. Lett.* **2013**, *4*, 908−918.
(7) Mora-Seró, I.; Giménez, S.; Fabregat-Santiago, F.; Gómez, R.; Shen, Q.; Toyoda, T.; Bisquert, J. Recombination in Quantum Dot Sensitized Solar Cells. *Acc. Chem. Res.* **2009**, *42*, 1848−1857.
(8) Jia, J.; Seitz, L. C.; Benck, J. D.; Huo, Y.; Chen, Y.; Ng, J. W. D.; Bilir, T.; Harris, J. S.; Jaramillo, T. F. Solar Water Splitting by Photovoltaic-Electrolysis with a Solar-to-Hydrogen Efficiency over 30%. *Nat. Commun.* **2016**, *7*, No. 13237.
(9) Kang, D.; Kim, T. W.; Kubota, S. R.; Cardiel, A. C.; Cha, H. G.; Choi, K. S. Electrochemical Synthesis of Photoelectrodes and Catalysts for Use in Solar Water Splitting. *Chem. Rev.* **2015**, *115*, 12839−12887.
(10) Das, A.; Han, Z.; Haghighi, M. G.; Eisenberg, R. Photogeneration of Hydrogen from Water Using CdSe Nanocrystals Demonstrating the Importance of Surface Exchange. *Proc. Natl. Acad. Sci. U.S.A.* **2013**, *110*, 16716−16723.
(11) Medintz, I. L.; Uyeda, H. T.; Goldman, E. R.; Mattoussi, H. Quantum Dot Bioconjugates for Imaging, Labelling and Sensing. *Nat. Mater.* **2005**, *4*, 435−446.
(12) Wolfbeis, O. S. An Overview of Nanoparticles Commonly Used in Fluorescent Bioimaging. *Chem. Soc. Rev.* **2015**, *44*, 4743−4768.
(13) Wegner, K. D.; Hildebrandt, N. Quantum Dots: Bright and Versatile in Vitro and in Vivo Fluorescence Imaging Biosensors. *Chem. Soc. Rev.* **2015**, *44*, 4792−4834.
(14) Michalet, X.; Pinaud, F. F.; Bentolila, L. A.; Tsay, J. M.; Doose, S.; Li, J. J.; Sundaresan, G.; Wu, A. M.; Gambhir, S. S.; Weiss, S. Quantum Dots for Live Cells, in Vivo Imaging, and Diagnostics. *Science* **2005**, *307*, 538−544.
(15) Hartley, C. L.; Kessler, M. L.; Dempsey, J. L. Molecular-Level Insight into Semiconductor Nanocrystal Surfaces. *J. Am. Chem. Soc.* **2021**, *143*, 1251−1266.
(16) Jasieniak, J.; Califano, M.; Watkins, S. E. Size-Dependent Valence and Conduction Band-Edge Energies of Semiconductor Nanocrystals. *ACS Nano* **2011**, *5*, 5888−5902.
(17) Hines, D. A.; Kamat, P. V. Recent Advances in Quantum Dot Surface Chemistry. *ACS Appl. Mater. Interfaces* **2014**, *6*, 3041−3057.
(18) Hens, Z.; de Roo, J. Atomically Precise Nanocrystals. *J. Am. Chem. Soc.* **2020**, *142*, 15627−15637.
(19) Kroupa, D. M.; Vörös, M.; Brawand, N. P.; McNichols, B. W.; Miller, E. M.; Gu, J.; Nozik, A. J.; Sellinger, A.; Galli, G.; Beard, M. C. Tuning Colloidal Quantum Dot Band Edge Positions through Solution-Phase Surface Chemistry Modification. *Nat. Commun.* **2017**, *8*, No. 15257.
(20) Zhou, Q.; Cho, Y.; Yang, S.; Weiss, E. A.; Berkelbach, T. C.; Darancet, P. Large Band Edge Tunability in Colloidal Nanoplatelets. *Nano Lett.* **2019**, *19*, 7124−7129.
(21) Cho, W.; Kim, S.; Coropceanu, I.; Srivastava, V.; Diroll, B. T.; Hazarika, A.; Fedin, I.; Galli, G.; Schaller, R. D.; Talapin, D. V. Direct Synthesis of Six-Monolayer (1.9 Nm) Thick Zinc-Blende CdSe Nanoplatelets Emitting at 585 Nm. *Chem. Mater.* **2018**, *30*, 6957−6960.
(22) Asokan, S.; Krueger, K. M.; Colvin, V. L.; Wong, M. S. Shape-Controlled Synthesis of CdSe Tetrapods Using Cationic Surfactant Ligands. *Small* **2007**, *3*, 1164−1169.
(23) Meyns, M.; Iacono, F.; Palencia, C.; Geweke, J.; Coderch, M. D.; Fittschen, U. E. A.; Gallego, J. M.; Otero, R.; Juárez, B. H.; Klinke, C. Shape Evolution of CdSe Nanoparticles Controlled by Halogen Compounds. *Chem. Mater.* **2014**, *26*, 1813−1821.
(24) Peng, X.; Manna, L.; Yang, W.; Wickham, J.; Scher, E.; Kadavanich, A.; Alivisatos, A. P. Shape Control of CdSe Nanocrystals. *Nature* **2000**, *404*, 59−61.
(25) Liu, L.; Zhuang, Z.; Xie, T.; Wang, Y. G.; Li, J.; Peng, Q.; Li, Y. Shape Control of CdSe Nanocrystals with Zinc Blende Structure. *J. Am. Chem. Soc.* **2009**, *131*, 16423−16429.
(26) Shan, W.; Song, J. J.; Luo, H.; Furdyna, J. K. Determination of the Fundamental and Split-off Band Gaps in Zinc-Blende CdSe by Photomodulation Spectroscopy. *Phys. Rev. B* **1994**, *50*, 8012−8015.
(27) Lunz, U.; Kuhn, J.; Goschenhofer, F.; Schüssler, U.; Einfeldt, S.; Becker, C. R.; Landwehr, G. Temperature Dependence of the Energy Gap of Zinc-blende CdSe and Cd 1− x Zn x Se Epitaxial Layers. *J. Appl. Phys.* **1996**, *80*, 6861−6863.
(28) Hartmann, L.; Kumar, A.; Welker, M.; Fiore, A.; Julien-Rabant, C.; Gromova, M.; Bardet, M.; Reiss, P.; Baxter, P. N. W.; Chandezon, F.; Pansu, R. B. Quenching Dynamics in CdSe Nanoparticles: Surface-Induced Defects upon Dilution. *ACS Nano* **2012**, *6*, 9033−9041.
(29) Yang, S.; Prendergast, D.; Neaton, J. B. Tuning Semiconductor Band Edge Energies for Solar Photocatalysis via Surface Ligand Passivation. *Nano Lett.* **2012**, *12*, 383−388.
(30) Elimelech, O.; Aviv, O.; Oded, M.; Banin, U. A Tale of Tails: Thermodynamics of CdSe Nanocrystal Surface Ligand Exchange. *Nano Lett.* **2020**, *20*, 6396−6403.
(31) Lin, Q.; Yun, H. J.; Liu, W.; Song, H. J.; Makarov, N. S.; Isaienko, O.; Nakotte, T.; Chen, G.; Luo, H.; Klimov, V. I.; Pietryga, J. M. Phase-Transfer Ligand Exchange of Lead Chalcogenide Quantum Dots for Direct Deposition of Thick, Highly Conductive Films. *J. Am. Chem. Soc.* **2017**, *139*, 6644−6653.
(32) Anderson, N. C.; Hendricks, M. P.; Choi, J. J.; Owen, J. S. Ligand Exchange and the Stoichiometry of Metal Chalcogenide Nanocrystals: Spectroscopic Observation of Facile Metal-Carboxylate Displacement and Binding. *J. Am. Chem. Soc.* **2013**, *135*, 18536−18548.
(33) Ben-Shahar, Y.; Scotognella, F.; Waiskopf, N.; Kriegel, I.; Dal Conte, S.; Cerullo, G.; Banin, U. Effect of Surface Coating on the Photocatalytic Function of Hybrid CdS-Au Nanorods. *Small* **2015**, *11*, 462−471.
(34) Čapek, R. K.; Lambert, K.; Dorfs, D.; Smet, P. F.; Poelman, D.; Eychmüller, A.; Hens, Z. Synthesis of Extremely Small CdSe and Bright Blue Luminescent CdSe/ZnS Nanoparticles by a Prefocused Hot-Injection Approach. *Chem. Mater.* **2009**, *21*, 1743−1749.
(35) Cho, J.; Jung, Y. K.; Lee, J. K.; Jung, H. S. Highly Efficient Blue-Emitting CdSe-Derived Core/Shell Gradient Alloy Quantum Dots with Improved Photoluminescent Quantum Yield and Enhanced Photostability. *Langmuir* **2017**, *33*, 3711−3719.
(36) Moreels, I.; Rainò, G.; Gomes, R.; Hens, Z.; Stöferle, T.; Mahrt, R. F. Band-Edge Exciton Fine Structure of Small, Nearly Spherical Colloidal CdSe/ZnS Quantum Dots. *ACS Nano* **2011**, *5*, 8033−8039.
(37) Boldt, K.; Kirkwood, N.; Beane, G. A.; Mulvaney, P. Synthesis of Highly Luminescent and Photo-Stable, Graded Shell CdSe/Cd XZn1-XS Nanoparticles by in Situ Alloying. *Chem. Mater.* **2013**, *25*, 4731−4738.
(38) Peng, X.; Schlamp, M. C.; Kadavanich, A. V.; Alivisatos, A. P. Epitaxial Growth of Highly Luminescent CdSe/CdS Core/Shell

https://doi.org/10.1021/acsomega.3c00324
ACS Omega 2023, 8, 11467−11478

Nanocrystals with Photostability and Electronic Accessibility. *J. Am. Chem. Soc.* **1997**, *119*, 7019−7029.
(39) Elimelech, O.; Aviv, O.; Oded, M.; Peng, X.; Harries, D.; Banin, U. Entropy of Branching Out: Linear versus Branched Alkylthiols Ligands on CdSe Nanocrystals. *ACS Nano* **2022**, *16*, 4308−4321.
(40) Gomes, R.; Hassinen, A.; Szczygiel, A.; Zhao, Q.; Vantomme, A.; Martins, J. C.; Hens, Z. Binding of Phosphonic Acids to CdSe Quantum Dots: A Solution NMR Study. *J. Phys. Chem. Lett.* **2011**, *2*, 145−152.
(41) Jose, R.; Zhanpeisov, N. U.; Fukumura, H.; Baba, Y.; Ishikawa, I. Structure-Property Correlation of CdSe Clusters Using Experimental Results and First-Principles DFT Calculations. *J. Am. Chem. Soc.* **2006**, *128*, 629−636.
(42) Singh, S.; Leemans, J.; Zaccaria, F.; Infante, I.; Hens, Z. Ligand Adsorption Energy and the Postpurification Surface Chemistry of Colloidal Metal Chalcogenide Nanocrystals. *Chem. Mater.* **2021**, *33*, 2796−2803.
(43) Csik, I.; Russo, S. P.; Mulvaney, P. Density Functional Study of Surface Passivation of Nonpolar Wurtzite CdSe Surfaces. *J. Phys. Chem. C* **2008**, *112*, 20413−20417.
(44) Virgili, T.; Calzolari, A.; Suárez López, I.; Ruini, A.; Catellani, A.; Vercelli, B.; Tassone, F. Hybridized Electronic States between CdSe Nanoparticles and Conjugated Organic Ligands: A Theoretical and Ultrafast Photo-Excited Carrier Dynamics Study. *Nano Res.* **2018**, *11*, 142−150.
(45) Virgili, T.; Calzolari, A.; Suárez López, I.; Vercelli, B.; Zotti, G.; Catellani, A.; Ruini, A.; Tassone, F. Charge Separation in the Hybrid Cdse Nanocrystal-Organic Interface: Role of the Ligands Studied by Ultrafast Spectroscopy and Density Functional Theory. *J. Phys. Chem. C* **2013**, *117*, 5969−5974.
(46) Manna, L.; Wang, L. W.; Cingolani, R.; Alivisatos, A. P. First-Principles Modeling of Unpassivated and Surfactant-Passivated Bulk Facets of Wurtzite CdSe: A Model System for Studying the Anisotropic Growth of CdSe Nanocrystals. *J. Phys. Chem. B* **2005**, *109*, 6183−6192.
(47) Azpiroz, J. M.; Ugalde, J. M.; Infante, I. Benchmark Assessment of Density Functional Methods on Group II-VI MX (M = Zn, Cd; X = S, Se, Te) Quantum Dots. *J. Chem. Theory Comput.* **2014**, *10*, 76−89.
(48) Azpiroz, J. M.; Matxain, J. M.; Infante, I.; Lopez, X.; Ugalde, J. M. A DFT/TDDFT Study on the Optoelectronic Properties of the Amine-Capped Magic (CdSe)13 Nanocluster. *Phys. Chem. Chem. Phys.* **2013**, *15*, 10996−11005.
(49) Gao, Y.; Zhou, B.; Kang, S. G.; Xin, M.; Yang, P.; Dai, X.; Wang, Z.; Zhou, R. Effect of Ligands on the Characteristics of (CdSe)13 Quantum Dots. *RSC Adv.* **2014**, *4*, 27146−27151.
(50) Swenson, N. K.; Ratner, M. A.; Weiss, E. A. Computational Study of the Influence of the Binding Geometries of Organic Ligands on the Photoluminescence Quantum Yield of CdSe Clusters. *J. Phys. Chem. C* **2016**, *120*, 6859−6868.
(51) Tan, L.; Pickard, C. J.; Yu, K.; Sapelkin, A.; Misquitta, A. J.; Dove, M. T. Structures of CdSe and CdS Nanoclusters from Ab Initio Random Structure Searching. *J. Phys. Chem. C* **2019**, *123*, 29370−29378.
(52) Inerbaev, T. M.; Masunov, A. E.; Khondaker, S. I.; Dobrinescu, A.; Plamad, A. V.; Kawazoe, Y. Quantum Chemistry of Quantum Dots: Effects of Ligands and Oxidation. *J. Chem. Phys.* **2009**, *131*, 044106.
(53) Cui, Y.; Cui, X.; Zhang, L.; Xie, Y.; Yang, M. Theoretical Characterization on the Size-Dependent Electron and Hole Trapping Activity of Chloride-Passivated CdSe Nanoclusters. *J. Chem. Phys.* **2018**, *148*, 134308.
(54) Cui, Y.; Lou, Z.; Wang, X.; Yu, S.; Yang, M. A Study of Optical Absorption of Cysteine-Capped CdSe Nanoclusters Using First-Principles Calculations. *Phys. Chem. Chem. Phys.* **2015**, *17*, 9222−9230.
(55) Sun, J.; Zheng, X.; He, H.; Chen, X.; Dong, B.; Fei, R. Theoretical Study of Ligand and Solvent Effects on Optical Properties and Stabilities of CdSe Nanoclusters. *J. Mol. Struct.* **2016**, *1114*, 123−131.
(56) Voznyy, O.; Mokkath, J. H.; Jain, A.; Sargent, E. H.; Schwingenschlögl, U. Computational Study of Magic-Size Cdse Clusters with Complementary Passivation by Carboxylic and Amine Ligands. *J. Phys. Chem. C* **2016**, *120*, 10015−10019.
(57) Liu, H. Tuning the Binding Energy of Surfactant to Cdse Nanocrystal: A Theoretical Study. *J. Phys. Chem. C* **2009**, *113*, 3116−3119.
(58) Nguyen, K. A.; Pachter, R.; Day, P. N. Computational Prediction of Structures and Optical Excitations for Nanoscale Ultrasmall ZnS and CdSe Clusters. *J. Chem. Theory Comput.* **2013**, *9*, 3581−3596.
(59) del Ben, M.; Havenith, R. W. A.; Broer, R.; Stener, M. Density Functional Study on the Morphology and Photoabsorption of CdSe Nanoclusters. *J. Phys. Chem. C* **2011**, *115*, 16782−16796.
(60) Azpiroz, J. M.; de Angelis, F. Ligand Induced Spectral Changes in CdSe Quantum Dots. *ACS Appl. Mater. Interfaces* **2015**, *7*, 19736−19745.
(61) Kilina, S.; Ivanov, S.; Tretiak, S. Effect of Surface Ligands on Optical and Electronic Spectra of Semiconductor Nanoclusters. *J. Am. Chem. Soc.* **2009**, *131*, 7717−7726.
(62) Ghosh, D.; Ivanov, S. A.; Tretiak, S. Structural Dynamics and Electronic Properties of Semiconductor Quantum Dots: Computational Insights. *Chem. Mater.* **2021**, *33*, 7848−7857.
(63) Albert, V. V.; Ivanov, S. A.; Tretiak, S.; Kilina, S. V. Electronic Structure of Ligated Cdse Clusters: Dependence on DFT Methodology. *J. Phys. Chem. C* **2011**, *115*, 15793−15800.
(64) Fischer, S. A.; Crotty, A. M.; Kilina, S. V.; Ivanov, S. A.; Tretiak, S. Passivating Ligand and Solvent Contributions to the Electronic Properties of Semiconductor Nanocrystals. *Nanoscale* **2012**, *4*, 904−914.
(65) Kilina, S. V.; Tamukong, P. K.; Kilin, D. S. Surface Chemistry of Semiconducting Quantum Dots: Theoretical Perspectives. *Acc. Chem. Res.* **2016**, *49*, 2127−2135.
(66) Kilina, S. V.; Kilin, D. S.; Prezhdo, O. V. Breaking the Phonon Bottleneck in PbSe and CdSe Quantum Dots: Time-Domain Density Functional Theory of Charge Carrier Relaxation. *ACS Nano* **2009**, *3*, 93−99.
(67) Giansante, C.; Infante, I. Surface Traps in Colloidal Quantum Dots: A Combined Experimental and Theoretical Perspective. *J. Phys. Chem. Lett.* **2017**, *8*, 5209−5215.
(68) du Fossé, I.; Boehme, S. C.; Infante, I.; Houtepen, A. J. Dynamic Formation of Metal-Based Traps in Photoexcited Colloidal Quantum Dots and Their Relevance for Photoluminescence. *Chem. Mater.* **2021**, *33*, 3349−3358.
(69) Houtepen, A. J.; Hens, Z.; Owen, J. S.; Infante, I. On the Origin of Surface Traps in Colloidal II-VI Semiconductor Nanocrystals. *Chem. Mater.* **2017**, *29*, 752−761.
(70) Drijvers, E.; de Roo, J.; Martins, J. C.; Infante, I.; Hens, Z. Ligand Displacement Exposes Binding Site Heterogeneity on CdSe Nanocrystal Surfaces. *Chem. Mater.* **2018**, *30*, 1178−1186.
(71) du Fossé, I.; Lal, S.; Hossaini, A. N.; Infante, I.; Houtepen, A. J. Effect of Ligands and Solvents on the Stability of Electron Charged CdSe Colloidal Quantum Dots. *J. Phys. Chem. C* **2021**, *125*, 23968−23975.
(72) Kuznetsov, A. E.; Beratan, D. N. Structural and Electronic Properties of Bare and Capped Cd 33Se33 and Cd33Te33 Quantum Dots. *J. Phys. Chem. C* **2014**, *118*, 7094−7109.
(73) Puzder, A.; Williamson, A. J.; Gygi, F.; Galli, G. Self-Healing of CdSe Nanocrystals: First-Principles Calculations. *Phys. Rev. Lett.* **2004**, *92*, 217401.
(74) Puzder, A.; Williamson, A. J.; Zaitseva, N.; Galli, G.; Manna, L.; Alivisatos, A. P. The Effect of Organic Ligand Binding on the Growth of CdSe Nanoparticles Probed by Ab Initio Calculations. *Nano Lett.* **2004**, *4*, 2361−2365.
(75) Sarkar, P.; Springborg, M. Density-Functional Study of Size-Dependent Properties of CdmSen Clusters. *Phys. Rev. B* **2003**, *68*, No. 235409.

https://doi.org/10.1021/acsomega.3c00324
ACS Omega 2023, 8, 11467−11478

(76) Kasuya, A.; Sivamohan, R.; Barnakov, Y. A.; Dmitruk, I. M.; Nirasawa, T.; Romanyuk, V. R.; Kumar, V.; Mamykin, S. V.; Tohji, K.; Jeyadevan, B.; Shinoda, K.; Kudo, T.; Terasaki, O.; Liu, Z.; Belosludov, R. V.; Sundararajan, V.; Kawazoe, Y. Ultra-Stable Nanoparticles of CdSe Revealed from Mass Spectrometry. *Nat. Mater.* **2004**, *3*, 99−102.
(77) Kresse, G.; Furthmüller, J. Efficient Iterative Schemes for Ab Initio Total-Energy Calculations Using a Plane-Wave Basis Set. *Phys. Rev. B* **1996**, *54*, 11169−11186.
(78) Kresse, G.; Hafner, J. Ab Initio Molecular Dynamics for Liquid Metals. *Phys. Rev. B* **1993**, *47*, 558−561.
(79) Perdew, J. P.; Burke, K.; Ernzerhof, M. Generalized Gradient Approximation Made Simple. *Phys. Rev. Lett.* **1996**, *77*, 3865−3868.
(80) Grimme, S. Accurate Description of van Der Waals Complexes by Density Functional Theory Including Empirical Corrections. *J. Comput. Chem.* **2004**, *25*, 1463−1473.
(81) Heras-Domingo, J.; Sodupe, M.; Solans-Monfort, X. Interaction between Ruthenium Oxide Surfaces and Water Molecules. Effect of Surface Morphology and Water Coverage. *J. Phys. Chem. C* **2019**, *123*, 7786.
(82) González, D.; Heras-Domingo, J.; Pantaleone, S.; Rimola, A.; Rodríguez-Santiago, L.; Solans-Monfort, X.; Sodupe, M. Water Adsorption on MO 2 (M = Ti, Ru, and Ir) Surfaces. Importance of Octahedral Distortion and Cooperative Effects. *ACS Omega* **2019**, *4*, 2989−2999.
(83) Blöchl, P. E.; Först, C. J.; Schimpl, J. Projector Augmented Wave Method: Ab Initio Molecular Dynamics with Full Wave Functions. *Bull. Mater. Sci.* **2003**, *26*, 33−41.
(84) Kresse, G.; Joubert, D. From Ultrasoft Pseudopotentials to the Projector Augmented-Wave Method. *Phys. Rev. B* **1999**, *59*, 1758−1775.
(85) Monkhorst, H. J.; Pack, J. D. Special Points for Brillouin-Zone Integrations. *Phys. Rev. B* **1976**, *13*, 5188−5192.
(86) Bader, R. F. W. A Quantum Theory of Molecular Structure and Its Applications. *Chem. Rev.* **1991**, *91*, 893−928.
(87) Henkelman, G.; Arnaldsson, A.; Jónsson, H. A Fast and Robust Algorithm for Bader Decomposition of Charge Density. *Comput. Mater. Sci.* **2006**, *36*, 354−360.
(88) Romanova, K. A.; Galyametdinov, Y. G.Quantum-Chemical Study of CdSe/CdS Core/Shell and CdSe/CdS/ZnS Core/Shell/Shell Quantum Dots with Different Layers Ratio. In *AIP Conference Proceedings*; AIP Publishing, 2021; Vol. *2380*, p 060001 DOI: 10.1063/5.0058295.
(89) Dudarev, S. L.; Botton, G. A.; et al. Electron-Energy-Loss Spectra and the Structural Stability of Nickel Oxide: An LSDA+U Study. *Phys. Rev. B* **1998**, *57*, 1505−1509.
(90) Mathew, K.; Sundararaman, R.; Letchworth-Weaver, K.; Arias, T. A.; Hennig, R. G. Implicit Solvation Model for Density-Functional Study of Nanocrystal Surfaces and Reaction Pathways. *J. Chem. Phys.* **2014**, *140*, 084106.
(91) Nosé, S. A Unified Formulation of the Constant Temperature Molecular Dynamics Methods. *J. Chem. Phys.* **1984**, *81*, 511−519.
(92) Hoover, W. G. Canonical Dynamics: Equilibrium Phase-Space Distributions. *Phys. Rev. A* **1985**, *31*, 1695−1697.
(93) Pettersen, E. F.; Goddard, T. D.; Huang, C. C.; Couch, G. S.; Greenblatt, D. M.; Meng, E. C.; Ferrin, T. E. UCSF Chimera - A Visualization System for Exploratory Research and Analysis. *J. Comput. Chem.* **2004**, *25*, 1605−1612.
(94) Frisch, M. J.; Trucks, G. W.; Schlegel, H. B.; Scuseria, G. E.; Robb, M. A.; Cheeseman, J. R.; Scalmani, G.; Barone, V.; Mennucci, B.; Petersson, G. A.; Nakatsuji, H.; Caricato, M.; Li, X.; Hratchian, H. P.; Izmaylov, A. F.; Bloino, J.; Zheng, G.; Sonnenberg, J. L.; Hada, M.et al. *Gaussian16* (Revision A.03), Gaussian Inc.: Wallingford CT, 2016.
(95) Weigend, F.; Ahlrichs, R. Balanced Basis Sets of Split Valence, Triple Zeta Valence and Quadruple Zeta Valence Quality for H to Rn: Design and Assessment of Accuracy. *Phys. Chem. Chem. Phys.* **2005**, *7*, 3297.
(96) Andrae, D.; Häußermann, U.; Dolg, M.; Stoll, H.; Preuß, H. Energy-Adjusted ab Initio Pseudopotentials for the Second and Third Row Transition Elements. *Theor. Chim. Acta* **1990**, *77*, 123−141.
(97) Barone, V.; Cossi, M. Quantum Calculation of Molecular Energies and Energy Gradients in Solution by a Conductor Solvent Model. *J. Phys. Chem. A* **1998**, *102*, 1995−2001.
(98) Cossi, M.; Rega, N.; Scalmani, G.; Barone, V. Energies, Structures, and Electronic Properties of Molecules in Solution with the C-PCM Solvation Model. *J. Comput. Chem.* **2003**, *24*, 669−681.
(99) Kaneta, A.; Adachi, S. Photoreflectance Study of Hexagonal CdSe. *J. Phys. D: Appl. Phys.* **1999**, *32*, 2337−2341.
(100) Janowitz, C.; Günther, O.; Jungk, G.; Johnson, R. L.; Santos, P. V.; Cardona, M.; Faschinger, W.; Sitter, H. Dielectric Function and Critical Points of Cubic and Hexagonal CdSe. *Phys. Rev. B* **1994**, *50*, 2181−2187.
(101) Ninomiya, S.; Adachi, S. Optical Properties of Cubic and Hexagonal CdSe. *J. Appl. Phys.* **1995**, *78*, 4681−4689.

https://doi.org/10.1021/acsomega.3c00324
ACS Omega 2023, 8, 11467−11478